Inspection of Prebaked Carbon Anodes Using Multi-Spectral Acousto-Ultrasonic Signals, Wavelet Analysis and Multivariate Statistical Methods

Moez Ben Boubaker[1], Donald Picard[2], Carl Duchesne[3], Jayson Tessier[4], Houshang Alamdari[5] and Mario Fafard[6]

[1]PhD student, Département de génie chimique,
[2]Research Assistant, Département de génie civil,
[3]Professor, Département de génie chimique,
[5]Professor, Département de génie des mines, de la métallurgie et des matériaux,
[6]Professor, Département de génie civil,
Aluminum Research Centre – REGAL, Université Laval, Quebec (Qc), Canada
[4]Manager, Pilot Zone Operations, Alcoa Primary Metals Smelting Center of Excellence, Deschambault (Qc), Canada
Corresponding author: carl.duchesne@gch.ulaval.ca

Abstract

Reduction cell operation in primary aluminum production is greatly influenced by the baked anodes properties. Producing consistent anode quality is more challenging nowadays due to the increasing variability of raw materials. Taking timely corrective actions to attenuate the impact of raw material fluctuations on anode quality is also difficult based on the core sampling and characterization scheme currently used by most anode manufacturers because it is applied on a very small proportion of the anode production (about 1%), and long-time delays are required for lab characterization. The objective of this work is to develop rapid and non-destructive methods for inspection of baked anodes. In past work, it was shown that acousto-ultrasonic signals collected from anode parts at different frequencies were sensitive to anode defects (pores and cracks) and this was validated qualitatively using X-ray computed tomography. This work attempts to improve the method by using multi-spectral excitation signals and by establishing quantitative relationships between the acousto-ultrasonic signals and defects extracted from tomography images using Wavelet Transforms and Partial Least Squares (PLS) regression. This results in shorter acquisition time and a more specific and robust model for anode inspection. The method performance is illustrated using samples collected from industrial scale anodes.

Keywords: Non-destructive testing; acousto-ultrasonic signals; CT-Scan images; PCA; PLS.

1. Introduction

The performance of acousto-ultrasonic techniques in detection of various defects in carbon anodes has been demonstrated in previous work using sequential acoustic excitation at different frequencies of anode slices followed by the analysis of the acoustic responses of the samples using Principal Component Analysis (PCA). The results were validated qualitatively using X-ray images collected from the slices [1]. However, this method needs to be improved and adapted for real time control in order to pave the way for industrial application. In particular, it is necessary to reduce the cycle time of the approach using sequential excitation and to further validate the method through a quantitative use of the X-ray CT scan images of the samples.

To reduce the cycle time, it is proposed to excite the materials using a single multi-frequency acoustic signal. However, this would lead to a more complex acoustic response of the anode samples requiring the use of some frequency decomposition techniques to extract from the response signals features at different frequencies. One approach consists of using the Fast-

Fourier transform (FFT) [2-5]. In this method, acousto-ultrasonic signals are decomposed in different frequency bands that can be used to identify various failure modes. However, time domain information cannot be extracted using FFT (i.e., variations in signal frequency content through time) and this may limit the performance in defect detection and identification. An alternative approach that is becoming increasingly popular in industrial applications consists of using the Wavelet Transforms (WTs) where both frequencies and time information can be obtained from acousto-ultrasonic signals [6-9]. In addition, WTs were shown to be a powerful tool in all areas dealing with transient signals [10-12]. Qi et al. [13, 14] showed the effectiveness of the Discrete Wavelet Transform (DWT) to process the acousto-ultrasonic signals from composite materials. A similar approach could be used for the analysis of baked carbon anode materials.

To validate the performance of the acousto-ultrasonic approach more precisely, it is also proposed to quantify defects from X-ray CT-scan images of the carbon anode samples and to establish a relationship between the features extracted from the acoustic response of the samples and the types of defects and their severity. To quantify defects in tomographic images image texture analysis techniques can be used since the defects introduce local variations in grey level intensity in the images according to some relatively well defined patterns (i.e., round spots for pores and streak lines for cracks). Again here, one could extract textural features from tomographic images using the two-dimensional Fast Fourier transform (2D-FFT) [15]. In this method, the frequency decomposition of the images could be used determine the severity of defects. However, variations in frequency content within the images (i.e., spatial information) cannot be extracted using this approach. On the other hand, the 2D Discrete Wavelet Transforms (2D-DWTs) are effective for extracting both frequency and spatial information could be obtained [16]. Moreover, wavelet texture analysis has been shown to be a powerful tool in several areas dealing with noise and low variation in images.

In order to build relationships between the acoustic response signals of the samples and their CT-scan images, multivariate statistical methods such as Principal Component Analysis (PCA) and Partial Least Squares (PLS) regression can be used [17], allowing a good classification of patterns in the case of several input data [18, 19]. These methods project a set of features from a higher to a lower dimensional space, simplifying the analysis of big data sets. Some authors [20, 21] have combined wavelet analysis and PCA, called Wavelet PCA, to improve the results of feature extraction. In order to correlate both acousto-ultrasonic and tomography images dataset blocks, Projection to Latent Structures (PLS) is implemented [22, 23].

This work aims at investigating the use of acousto-ultrasonic technique for volumetric inspection of baked carbon anodes. It focuses on mapping morphological constituents in this carbon material in order to evaluate spatial distribution of pores and cracks using acousto-ultrasonic wave attenuation. In this approach, an industrial baked anode was sliced along its length and some slices were used as real samples. The latter was scanned by X-Ray tomography and the resulting images were analyzed by wavelet to reveal the internal structure. Further, several acousto-ultrasonic features were extracted from the signals propagated through the corresponding parts using wavelet analysis. To simplify the analysis, both PCA and PLS were used to provide classification and regression models. The clustering patterns show the good potential of the proposed approach to detect and distinguish the pores from cracks.

2. CT-scan and acousto-ultrasonic set-up

2.1. X-Ray computed tomography data acquisition

A whole industrial baked carbon anode was scanned using Siemens Somatom Sensation 64 tomograph. Since this apparatus has been designed for human body, the anode block was too large to be scanned in one step. The anode was thus cut in several slices. Furthermore, smaller sample size increases the image resolution of a single scan, consequently the contrast between defects and background increases [24]. The anode was first cut into 26 thin parts (Figure 1 left) and then all slices were cut further in halves along their heights (Figure 1 right).

The CT-scan provides a 3D voxel matrix (1000×1200×10000) with attenuation coefficients varying between 0 and 4095. The intensity of the voxels (CT numbers) was converted to grayscale images as it is correlated to the materials density [24, 25]. Cracks and pores appear as groups of dark pixels surrounded by lighter background. The high-density impurities appear as bright pixels inside a darker background (Figure 2).

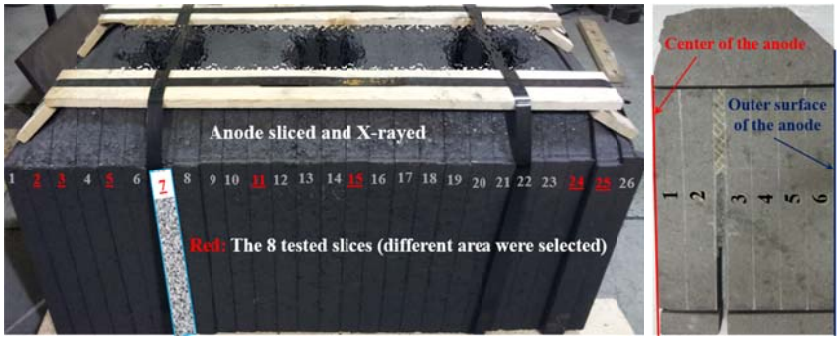

Figure 1. The sliced baked anode. Left: the selected 8 slices are identified in red. Right: example of a slices used for acousto-ultrasonic testing.

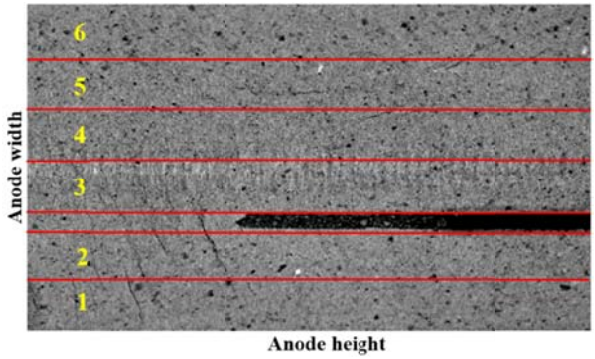

Figure 2. The appearance of the obtained X-ray images of an anode sample.

2.2. Acousto-ultrasonic signal acquisition

An overview of the acousto-ultrasonic signal measurement system and acquisition setup have been reported in [1]. In the present work, the input excitation signals were specified as a modulated frequency signal between 100 and 300 KHz as shown in Figure 3. This range was chosen based on the preliminary tests. The procedure was repeated for all six corridors (Figure 1 right) of each anode slice.

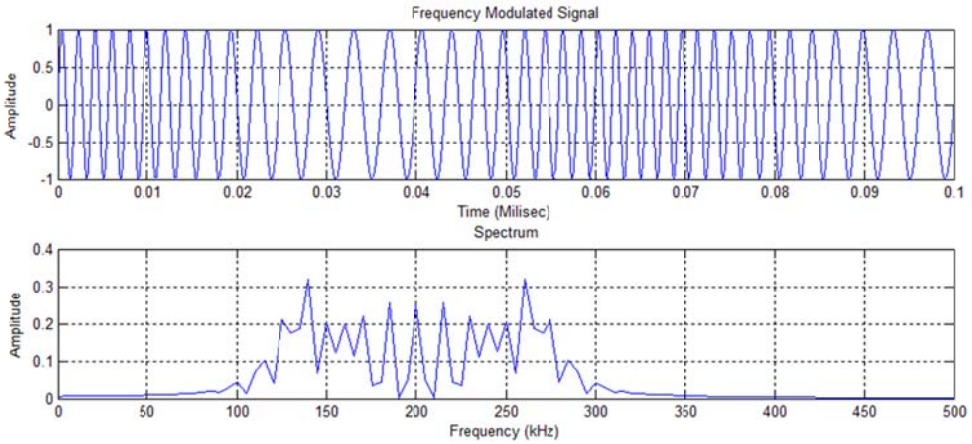

Figure 3. Frequency modulated waveform used as the excitation signal. Both the time series (top) and the frequency content (bottom) of the signal are shown.

3. Analysis of acoustic signals and X-ray images

3.1. Acousto-ultrasonic signals

The majority of the acousto-ultrasonic signals that can propagate in porous materials are concentrated in the frequency range of 10-300 kHz. Dividing this range into a set of consecutive frequency bands may be useful in associating different time-frequency features of acousto-ultrasonic signals to various defects in porous materials. To decompose the signal in different frequency bands, band pass filters [18] and Fourier Transforms [14, 26] can be used. However, as mentioned earlier, these techniques have no time resolution and may fail to detect small local disturbances in acoustic signals associated with some defects. Hence, wavelet transforms are used to decompose the signals into time-frequency domain.

The decomposition of a continuous 1D signal x(t) using a specific scaled or dilated mother wavelet ψ(t,a,b) is obtained by the convolution of both the signal and the wavelet function as follows [27]:

$$d_{a,b} = \frac{1}{\sqrt{a}} \int_{-\infty}^{+\infty} x(t)\, \psi\left(\frac{t-b}{a}\right) dt \qquad (1)$$

In the above equation, ψ(•) is the mother wavelet function which corresponds to a wave of finite length and having a particular shape. Several types of mother wavelet exist (e.g., Haar, Daubechies, Coiflet, Symlet, Mexican Hat, etc.), and they mainly differ by their shape (frequency content). The type of mother wavelet is typically selected so as to match the shape of the signal x(t) the best possible. The Daubechies wavelet (Db5) was selected in this work. This choice came after selecting the best results from trying several different mother wavelets. Parameters a and b are integers and are called the scaling and the translation parameters, respectively. The former stretches the mother wavelet and changes its frequency content while the latter performs a translation of the wavelet over time. The results of the convolution is a scalar quantity $d_{a,b}$, called the wavelet detail coefficient, and represents how well the signal x(t) matches the dilated mother wavelet at scale a and time point b. Changing the scaling coefficient a from a small to a large value progressively dilates the wavelet and therefore allows extracting information about signal x(t) from high to low frequency. Translating the wavelet using parameter b from the beginning to the end of the x(t) signal allows capturing information at different time points. Hence, changing a and b in a nested fashion performs a spatial-frequency

decomposition of signal x(t) and how well the signal matches at wavelet at scale a and time point b is quantified by the detail coefficient $d_{a,b}$. Note that the acoustic signals analysed in this work are discrete (i.e., sampled at a given frequency). A discrete version of equation 1 exist for discrete signals as well. This leads to the so-called Discrete Wavelet Transform (DWT). Values taken by the a and b parameters are constrained for computing efficiency and to avoid signal aliasing.

After performing the wavelet decomposition of signal x(t), a set of vectors of detail coefficients $d_a(t)$ is obtained, one for each scale a. Each vector contains the detail coefficient at a given scale but for all time points. In other words, the original signal x(t) is decomposed into a set of detail signals $d_a(t)$, each containing information about a certain frequency band. Three time domain features were then calculated from each time series $d_a(t)$, t=1,2,…N, N being the number of samples in the time series. These features are the maximum (MAX), the root mean square (RMS) and the time of flight, or arrival time (AT). These features are calculated as follows:

$$MAX_a = \max_{i=1}^{N} d_a(t) \tag{2}$$

$$RMS_a = \sqrt{\frac{1}{N}\sum_{i=1}^{N}\left[d_a(t)\right]^2} \tag{3}$$

$$AT_a = t \quad \text{when} \quad d_a(t) \geq 0.15 \times \max(d_a(t)) \tag{4}$$

The acoustic response of the materials x(t) was decomposed up to level 4 (four different discrete values of a) and the MAX and RMS features were calculated from each of them as well as the arrival time. Figure 4 provide an example of a raw acoustic signals decomposed into 4 frequency bands (details 1-4) and also shows the residual signal after four decomposition levels (called approximation).

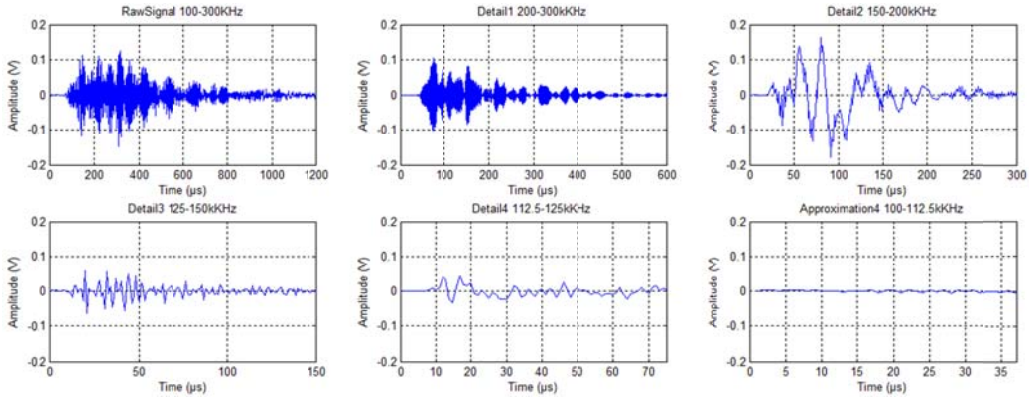

Figure 4. Example wavelet decomposition of an acoustic signal using 4 decomposition levels. The raw signal, the 4 wavelet detail signals as well as the residuals (approximation) are presented.

The data were then collected in a (56×15) dimensional matrix **X**. The 15 columns correspond to the three features computed from the 4 wavelet detail signals as well as the approximation for all of the 56 samples (7 corridors × 8 anode slices). Signal and image processing were performed using Matlab version R2014a (MathWorks, Natick, MA, USA).

3.2. X-ray image texture analysis

The texture of X-ray images was analysed using a very similar approach as for the acoustic signals. The tomography data were first converted to grayscale images. The Discrete Wavelet

Transform was then applied to the images. The main difference in the application of wavelets to images and acoustic signals is that images are 2D signals. An image is a matrix of data I(X,Y) where X and Y are the number of pixels in the horizontal and vertical directions of the images and the elements of that matrix correspond to the X-ray attenuation coefficients converted to grayscale values. The convolution between a mother wavelet and the image signals (i.e., discretized version of equation 1) is performed along each row and each column of the image (horizontally and vertically) as well as diagonally. Wavelet detail coefficients are obtained for each pixel of the images at each scale and for each of the three directions. These are collected into matrices D_j^k where j correspond to the scale, k to each direction (h,v,d), and each element of these matrices to the detail coefficient at a certain pixel location (x,y). These matrices can be shown as images as well for visual interpretation are typically called wavelet detail sub-images (D_j^h, D_j^v, D_j^d). At the first scale, high frequency information is captured from the images in all three directions and these are associated with small objects or patterns in the image. As the scale increases, lower frequency information introduced by larger objects or patterns are extracted. The 5th order Daubechies wavelet (Db5) wavelet was selected for analysing the texture of X-ray images.

Several scalar textural descriptors or textural features can be calculated from the wavelet detail sub-images, the most popular being the energy, variance, entropy, and the mean [28-29]. Our results showed that the energy is sufficient to extract information related with anode defects (pores and cracks) with the X-ray images. The energy is calculated as follows from the wavelet detail sub-images at each scale and for the three directions:

$$E_j^k = \frac{\sum_{x=1}^{X}\sum_{y=1}^{Y}\left|d_j^k(x,y)\right|^2}{X\,Y} \tag{5}$$

Where d_j^k is the detail coefficient for pixel located at the (x,y) position within an image in the kth direction (k = h, v, d) and the the jth scale. The total number of pixel within the images (XY) is used to normalize the energy values. The X-ray images were decomposed up to scale 4. This yields 12 energy values per anode corridor (4 scales × 3 directions). These values were collected for the 56 corridors and stored in matrix **Y** of dimensions (56×12).

The application of wavelet decomposition to one such X-ray image is shown on Figure 5. It shows the original image as well as the detail sub-images for each of the 4 scales and directions. The sub-images are identified by the direction first (h,v,d) and then by the scale number (1,2,3,4). For instance sub-images v3 displays the information extracted from the image by the wavelet in the vertical direction at scale 3. The vertical and diagonal sub-images at scales 2-4 clearly capture the profile line of the vertical and diagonal cracks in the image. This information will be regressed against the acoustic signals in order to link the acoustic attenuation to anode defects quantitatively.

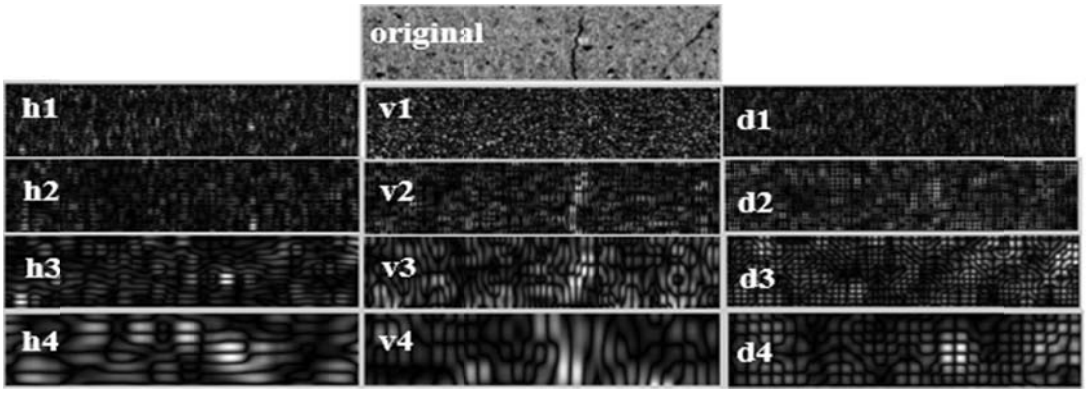

Figure 5. 2D Discrete wavelet decomposition of an X-ray image at 4 scales and in 3 directions. The wavelet sub-images are identified by the direction of analysis (h,v,d) followed by the scale number (1-4).

4. Multivariate statistical methods

Multivariate statistical methods are used to analyze the large data matrices obtained in this study. First, Principal Component Analysis (PCA) is used to cluster the X-ray images based on their texture (**Y** data). Then, Partial Least Squares (PLS) regression is used to build relationships between the acoustic attenuation data (**X**) and then image textural features (**Y**). These methods are briefly described below.

4.1. Principal Component Analysis (PCA)

Data clustering in the latent variable space using methods such as PCA is widely used for the analysis of large datasets containing noisy and highly collinear data. PCA summarizes the variations contained in a large set of J variables $\mathbf{X}=[\mathbf{x}_1, \mathbf{x}_2,\ldots, \mathbf{x}_J]$ by a much smaller number of orthogonal latent variables (or scores) $\mathbf{T}=[\mathbf{t}_1, \mathbf{t}_2,.., \mathbf{t}_A]$ (A<<J) together capturing the dominant sources of variations in the data. The scores are obtained by an eigenvector-eigenvalue bilinear decomposition of the **X** matrix and is mathematically expressed as follows [30, 31]:

$$\mathbf{X} = \sum_{a=1}^{A} \mathbf{t}_a \, \mathbf{p}_a^T + \mathbf{E} = \mathbf{T}\mathbf{P}^T + \mathbf{E} \qquad (6)$$

where the orthogonal vectors $\mathbf{t}_a$ are the latent variables (called scores) providing the coordinates of each sample in the low dimensional subspace (plane or hyperplane) after projection. The subspace itself is defined by the A orthonormal loading vectors $\mathbf{p}_a$, which are linear combinations of the original variables (i.e. $\mathbf{t}_a = \mathbf{X}\,\mathbf{p}_a$). The projection residuals are collected in the residual matrix **E**. The loading vectors are calculated in such a way that $\mathbf{t}_1$ explains the greatest amount of variance in **X**, $\mathbf{t}_2$ the second greatest amount of variance not being explained by the first component, and so on. Plots of the score values are used to visualize the clustering pattern of the data while the loadings allow interpretation of the patterns by the changes in the variables.

4.2. Partial Least Squares (PLS) regression

The PLS regression method is used to correlate the acousto-ultrasonic features of the anode corridors gathered in **X** matrix with corresponding image textural features collected in **Y**. Similar as for PCA, this regression method has an advantage of overcoming the strong

correlation between features in both data blocks. Each PLS latent variable is calculated in such as was to maximize the covariance in both data matrices and the following model structure is obtained [22-23]:

$$\mathbf{X} = \mathbf{TP}^{\mathbf{T}} + \mathbf{E} \quad (7)$$

$$\mathbf{Y} = \mathbf{TC}^{\mathbf{T}} + \mathbf{F} \quad (8)$$

$$\mathbf{T} = \mathbf{XW}^{*} = \mathbf{XW}(\mathbf{P}^{\mathbf{T}}\mathbf{W})^{-1} \quad (9)$$

where the latent variable space of both **X** and **Y** correspond to the scores **T** (orthogonal PLS components) which related **X** to **Y**. The sub-spaces of **X** and **Y** are modelled by the loading matrices **P** and **C**, respectively, while the corresponding residuals are stored in **E** and **F**. Finally, the so-called weight vectors **W*** contains the linear combinations that expresses **T** in terms of **X** and allow to make predictions of **Y**.

PCA and PLS effectively perform unsupervised clustering of samples vector in the latent variable subspace, which can be visualized using scatter plots of the scores (**t**'s). The differences between the clusters can be interpreted using the loading vectors (**p**'s). The reader is referred to Wold et al. [23] for more details about these methods. The ProMV software version 15.08 (ProSensus, Ancaster, ON, Canada) was used to build PCA and PLS models.

5. Results and discussion

5.1. Classification of the corridors based on X-ray images

Using the cross-validation procedure [32], two PCA components (or latent variables) were found significant and together explain most of the variations in the image textural features. The cumulative sum of squares explained (R^2) and predicted (Q^2) by the first two PCA components are provided in Table 1. The reader is referred to [31] for more details on PCA. The first two components were found sufficient to discriminate the corridors based on their textural features since they explain over 83% of variance inside those features (Q^2=83.21% in Table 1).

Table 1. Percent cumulative sum of squares explained (R^2) and predicted (Q^2) by the PCA model built on textural features collected from anode slices X-ray images.

Component	R^2 (%)	Q^2 (%)
1	60,3	58,7
2	84	83.21

The main variability directions in the image dataset captured by the two PCA components are presented in the t_1-t_2 score plot shown in Figure 6. Each marker in this plot represents a summary of the textural features of one particular corridor. These were identified by the slice number followed by the corridor number. Corridors having similar textural features cluster close to each other while those having different features cluster in different locations in the latent variable space. It is noticeable that the corridors located in the same position within the slices cluster together. Furthermore, each group is separated from others according to both components except those of slice number 25 that seem different from the others. This slice (#25) is located close to the corner of the anode block, and contains larger pores and cracks which makes then look like either corridors #1-2, typically containing several cracks, or to corridors #6 that contain lots of pores. This explain why the corridors of slide #25cluster close to corridors #1-2 or #6.

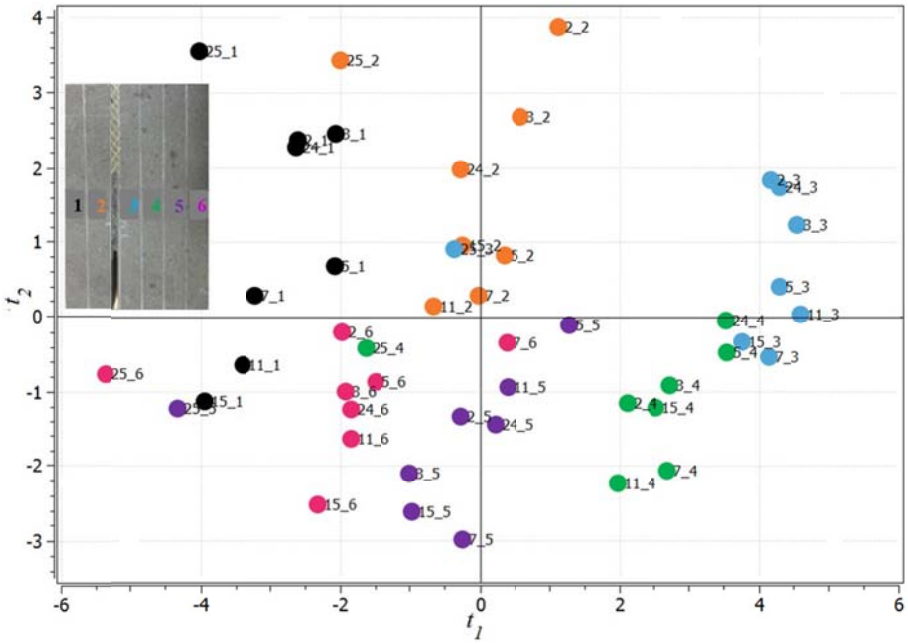

Figure 6. Score plot of the PCA model (t_1-t_2) showing the clustering pattern of the corridors in each slice based on their textural features extracted from X-ray images.

The clustering pattern in the score space can be related with changes in the textural features by examining the p_1-p_2 loading plot shown in Figure 7. Each point in the loading plot corresponds to one textural feature calculated from the image of each corridor. They are labeled according to the feature name followed by the wavelet decomposition level. The loading values define the weight of each textural features in each component. The higher the absolute value of the loadings the more important the features are in a given component. The sign of the loadings indicates the sign of their correlation. Features having loading values of the same sign are positively correlated and those having opposite signs are negatively correlated. The loading plot reveals that the first component is driven by most decomposition levels and all of them have loading values of the same sign (i.e., vary all together in the same direction). This component seems to explain variations in density across the X-ray images. A denser region is characterized by higher CT numbers and hence by higher grey levels in the image. This typically leads to higher energy values as calculated from the wavelet texture analysis. Since corridors 3-4 (and 5 to some extent) are known to be denser, it is expected that these corridors would fall in the positive t_1 region (see Figure 6) because the energies at all scales and directions would be higher. On the contrary, corridors 1-2 and 6 typically contain more defects (cracks and pores) and therefore are less dense. Hence, lower CT numbers, grey level intensities and energies. Thus, it is expected that these would fall in the negative t_1 region of the score plot. The second component, however, captures a contrast between the energies at scales 1-2 vs 3-4 since these two groups have loading values of opposite signs. This component seems to capture textural variation that corresponds to the defects sizes. Corridors containing larger defects (e.g., cracks) should be characterized by higher energies at higher scales (3-4) and lower energy at lower scales (1-2) since higher scales correspond to lower frequency content and larger objects or patterns. Since corridors 1-2 typically contain more cracks they fall in the positive t_2 region (higher energies at scales 3-4 and lower at scales 1-2). The situation is opposite with corridor 6 typically containing pores (clusters in negative t_2 region). Hence, the proposed wavelet texture analysis of X-ray images seems to capture variations in density and to discriminate between small and large defects in the anode samples (i.e., pores vs cracks).

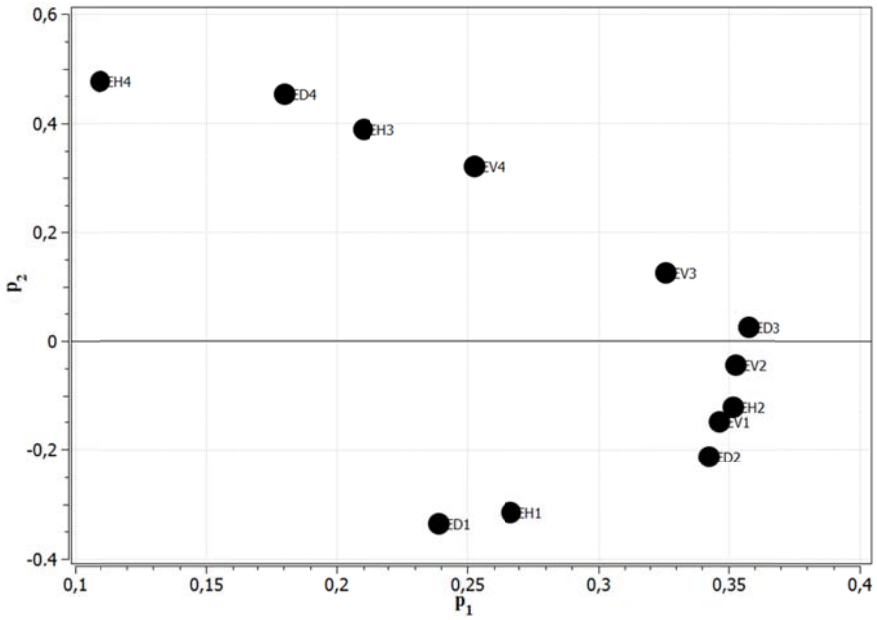

Figure 7. p_1-p_2 loading plot of the PCA model built on image textural features.

5.2. Regression of acousto-ultrasonic and textural features

Five PLS components were found statistically significant by a standard cross-validation procedure [32]. However, the first two were found sufficient in number to discriminate samples based on their acousto-ultrasonic signals. The latent variable score space for the first two components of the PLS model is displayed in Figure 8. Each marker in the plot corresponds to the acousto-ultrasonic response of one corridor which are identified by slice#_corridor#. The clustering pattern in the t_1-t_2 score space reveals that corridors 1-2, 3-5 and 6 of any slice cluster in 3 groups (black, orange and blue markers, respectively). At this point, it is important to remind that corridors #1 are located at the center of the anode and corridors #6 at the outer surface. It can also be observed that the attenuation features of corridors 1-2 and 6 seem more variable than the majority features of corridors 3-5 (orange cluster tighter than black and blue).

Now the internal structure of the corresponding samples analyzed in the previous section (PCA applied to X-ray image texture) is required to interpret the differences between these three groups. The first component (t_1) in Figure 8 seem to capture the types of the defects in the materials since the corridors where most of the cracks are found (1-2) are located in the negative t_1 region, those characterized by high concentration of pores (corridor 6) are located in the positive t_1 region, and corridors 3-5 fall in between the two. The second direction, which is orthogonal to the first, is sensitive to the severity of the defects (size of cracks and pores) as the denser corridors (some of corridors 3-5) are located above the more porous corridors (1-2 and 6) and the more cracked corridors (slice #5 and #7 located in the region under the stubs) are located above others. This is also in agreement with carbon plant knowledge. The region below the stub holes, corresponding to the corridors 1-2 (black cluster) in slices #5, 7 and 15, are generally expected to show a higher concentration of cracks when obviously some others, as in the slice #11, project closer to the denser region (orange markers). However, corridor 6 undergo a phenomenon of friction due to a lack of lubrication in vibro-compactor walls and consequently show typically high concentration of pores and project around blue markers, except slices #24 and 25 located in the anode corner (close to two outer surfaces).

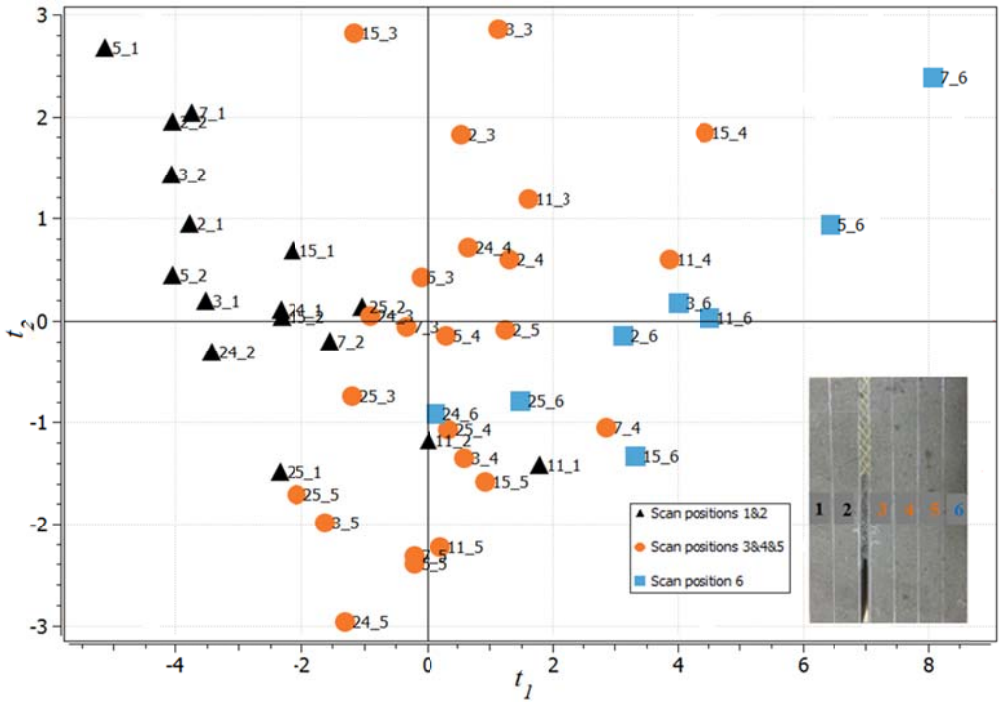

Figure 8. Score plot of the PLS model (t_1-t_2) between acoustic attenuation signals and X-ray image textural features.

The explanation of the relationship between acousto-ultrasonic attenuation features and the clustering pattern in the latent variable space is now interpreted using the w_1^*-c_1 − w_2^*-c_2 loadings bi-plot shown in Figure 9. The latter can be interpreted simultaneously with the t_1-t_2 score plot (Figure 8). The sign of X-loadings (w*'s - black markers in Figure 9) indicate the correlation sign between pairs of features whereas their absolute values give the information about the importance of the feature in a given component. It is observed that the first component is mainly driven by the variance related features (MAX and RMS) and the arrival time. The arrival time is negatively correlated to variance features because waves propagating through denser materials will have a shorter arrival time while the signals are less attenuated (higher MAX and RMS), and vice-versa. The clustering pattern along t_1 shows that this component discriminates the corridors containing more cracks (1-2), from the denser region (corridors 3-5) and corridor 6 containing more porosity. In the second component (t_2), all the features have the same loading sign meaning that they are all positively correlated. In addition, the loadings of the textural features (red squares in Figure 9) indicate a spread of the textural features at different scales from scale 1 to 4 from bottom to top of the plot (in the increasing t_2 direction). This suggests that the second component is sensitive to the size of the defects (larger in the positive t_2 region).

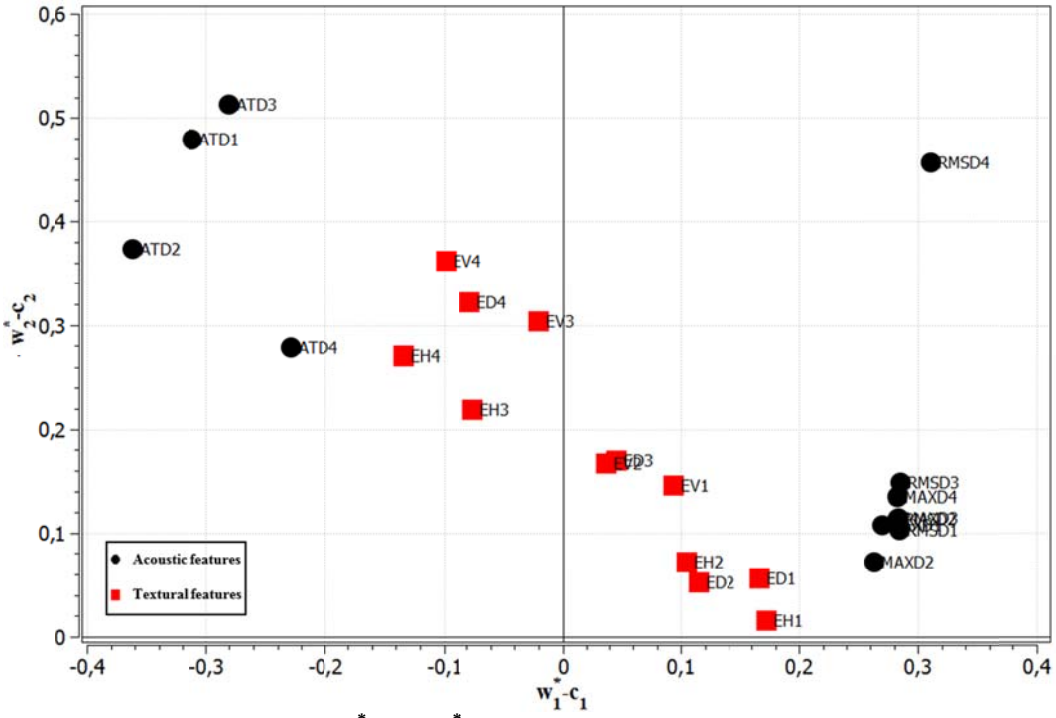

Figure 9. Loadings bi-plot (w_2^*-c_1 – w_2^*-c_2) of the PLS model between acoustic attenuation signals and X-ray image textural features.

It is also possible to interpret the correlation between the acousto-ultrasonic attenuation features and the textural image features using Figure 9. The fact that the energies at scales 3 and 4 (lower frequency content or larger objects) fall in the vicinity of the arrival times and opposite to variance related features confirm that corridors falling in the negative t_1 region in Figure 8 contain more severe defects, such as cracks, as opposed to those falling in the positive t_1 region which contain defects that attenuate the signal to a lesser extent (i.e. pores). This component therefore seems to discriminate between the types of defects. As explained earlier, the second component focuses on defect size, the larger de size, the more attenuated the acoustic signals are.

6. Conclusion

In this investigation, multispectral acousto-ultrasonic techniques, combined with multivariate statistical methods, were used in an attempt to quickly reveal the internal physical morphology of a full-scale anode, which was sliced in both longitudinal and transversal directions. Such combination has shown that multispectral signals features are sensitive to the presence of cracks within anode samples (measured by overall signal attenuation) and to the density of pores distributed throughout the block. Furthermore, CT-scan image analysis was used as a reference for quantitative validation of the observations made from the acousto-ultrasonic signal features and correlating them with internal morphology of the anode.

Besides, the non-destructive nature and the rapidity are the extra advantages of this technique. Based on these advantages and the obtained results, it can be concluded that the proposed approach appears very promising for a real-time quality control of industrial scale prebaked anodes.

7. References

1. M. Ben Boubaker et al., The Potential of Acousto-Ultrasonic Techniques for Inspection of Baked Carbon Anodes, *Metals*, Vol. 6, No. 7, 151, (2016), 1-13.
2. M. Suzuki, H. Nakanishi, and M. Iwamoto, Relationship between acoustic emission characteristics and structural factors of composite materials. Composites '86: Recent Advances in Japan and the United States, Proceedings of Japan–US CCM-III, Tokyo, 1986, 631–638.
3. N. Qing-Qing and J. Eiichi, Acoustic emission and fracture of carbon fiber reinforced thermosoftening plastic (CFRTP) materials under monotonous tensile loading, *Engineering Fracture Mechanics*, Vol. 45, No. 5, (1993), 611–625.
4. N. Qing-Qing and J. Eiichi, Fracture behavior and acoustic emission of SFC, *Journal of the Society of Materials Science*, Vol. 42, (1993), 561–567.
5. E. Jinen, Acoustic emission technique in the single-filament-composite test. *In: First International Conference on Composite Engineering (ICCE/1)*, August 28-31, Louisiana, New Orleans, USA, (1994), 883–884.
6. E.P. Serrano and M.A. Fabio, Application of the wavelet transform to acoustic emission signal processing, *IEEE Transactions on Signal Processing*, Vol. 44, No. 5, (1996), 1270–1275.
7. H. Suzuki et al., Wavelet transform of acoustic emission signals, *Journal of Acoustic Emission*, Vol. 14, No. 2, (1996), 69–84.
8. N. Qing-Qing and Y. Misada, Analysis of AE signals by wavelet transform, *Journal of the Society of Materials Science*, Vol. 47, (1998), 305–311.
9. L. Cohen, *Time–frequency analysis*, Prentice-Hall, Englewood Cliffs, NJ (1995).
10. R. Kronland-Martinet, J. Morlet, and A. Grossmann, Analysis of sound patterns through wavelet transforms, *International Journal of Pattern Recognition and Artificial Intelligence*, Vol. 1, No. 2, (1987), 273-302.
11. J.D. Aussel and J.P. Monchalin, Structure noise reduction and deconvolution of ultrasonic data using wavelet decomposition (ultrasonic flaw detection), *Proceedings of Ultrasonics Symposium*, Montreal, Canada, IEEE 1989, 1139-1144.
12. R.S. Loe et al., Status report on wavelets in signal detection and identification: comparative processing and technology evaluation, *Proceedings of IEEE Sixth SP Workshop on Statistical Signal and Array Processing*, Susono, Japan, 1992, 46-49.
13. G. Qi et al., Discrete wavelet decomposition of acoustic emission signals from carbon-fiber reinforced composites, *Composites Science and Technology*, Vol. 57, No. 4, (1997), 389–403.
14. G. Qi, Wavelet-based AE characterization of composite materials, *NDT & E International*, Vol. 33, No. 3, (2000), 133–145.
15. N. Sandirasegaram and R. English, Comparative analysis of feature extraction (2D FFT and wavelet) and classification (L_p metric distances, MLP NN, and HNeT) algorithms for SAR imagery, *Proceedings of SPIE 5808, Algorithms for Synthetic Aperture Radar Imagery XII,* Orlando, Florida (USA), March 28 2005, 314-325.
16. S.G. Mallat, A theory for multiresolution signal decomposition: the wavelet representation, *IEEE Transactions on Pattern Analysis and Machine Intelligence*, Vol. 11, No. 7, (1989), 674-693.
17. L. Eriksson et al, *Multi and megavariate data analysis: Part I: basic principles and applications*, 2nd ed., Umetrics Academy, Umea, Sweden, (2006).
18. M. Cherfaoui et al., The study of acoustic emission from composites by means of multivariate data analysis, *In: 6th International Conference on Composite Materials, and 2nd European Conference on Composite Materials*, London, England, (1987), 424-432.
19. M. Cherfaoui, A. Lemascon, and J. Roget, Detection and evaluation of defects in acoustic emission monitoring of bending tests". *In Eighth International Acoustic Emission Symposium*, Vol. 3, Tokyo, Japan, (1986), 586-593.

20. M. R. Gupta and N. P. Jacobson, Wavelet principal component analysis and its application to hyperspectral images, *In: IEEE International Conference on Image Processing*, Atlanta, GA, USA, October 8-11 2006, 1585-1588.
21. K. Tong, Wavelet transform and principal component analysis based feature extraction, Department of Mathematics, University of Washington, Seattle, WA, USA, June 3 2010. (http://www.math.washington.edu/~morrow/336_10/papers/kent.pdf last access August 24, 2016).
22. A. Höskuldsson, PLS regression methods, *Journal of Chemometrics*, Vol. 2, No. 3, (1988) 211-228.
23. S. Wold, M. Sjöström, and L. Eriksson, PLS-regression: a basic tool of chemometrics, *Chemometrics and Intelligent Laboratory Systems*, Vol. 58, No. 2, (2001), 109-130.
24. X. Boespflug et al., Axial tomodensitometry – relation between the Ct intensity and the density of the sample, *Canadian Journal of Earth Sciences*, Vol. 31, No. 2, (1994), 426-434.
25. D. Picard et al., Characterization of a full-scale prebaked carbon anode using x-ray computerized tomography, *Light Metals* 2011, 973-978.
26. K. Ono, J.S. Jeng, and J.M. Yang, Fracture mechanism studies of a carbon fiber-PEEK composite by acoustic emission, *In: Acoustic Emission: Current Practice and Future Directions*, ASTM International, Philadelphia, PA, (1991), 395-403.
27. K. Yamaguchi et al., Acoustic emission waveform characteristics from FRP during tensile test, *In: Progress in Acoustic Emission III, Proceedings of the 8th International Acoustic Emission Symposium (IAES 8)*, JSNDI, Tokyo, Japan, (1986), 594-601.
28. S. Borah, E.L. Hines, and M. Bhuyan, Wavelet transform based image texture analysis for size estimation applied to the sorting of tea granules, *Journal of Food Engineering*, Vol. 79, No. 2, (2007), 629-639.
29. M.H. Bharati, J.J. Liu, and J.F. MacGregor, Image texture analysis: methods and comparisons, *Chemometrics and Intelligent Laboratory Systems*, Vol. 72, No. 1, (2004), 57-71.
30. P. Geladi, H. Grahn, *Multivariate image analysis*, John Wiley & Sons, (1996).
31. S. Wold, K. Esbensen, and P. Geladi, Principal component analysis, *Chemometrics and Intelligent Laboratory Systems*, Vol. 2, No. 1-3, (1987), 37-52.
32. S. Wold, Cross-validatory estimation of the number of components in factor and principal component models, *Technometrics*, Vol. 20, No. 4, (1978), 397-405.